

Toward Reconfigurable Two-Bit Microwave Chiral Rasorbers

Yubo Wang^{1,2}, Xinyu Jiang^{1,2}, Pankaj K. Choudhury^{1,2}, and Yungui Ma^{1,2,*}

¹State Key Lab of Modern Optical Instrumentation, Centre for Optical and Electromagnetic Research
College of Optical Science and Engineering, Zhejiang University, Hangzhou 310058, China

²International Research Center for Advanced Photonics (Haining Campus), Zhejiang University, Hangzhou 310058, China

ABSTRACT: Reconfigurability is a crucial capability for electromagnetic devices to achieve high flexibility in accommodating various scenarios. In this study, we present a reconfigurable microwave rasorber with dynamically tunable helicity polarization for the passband wave using a compound unit cell composed of two-bit chiral meta-atoms. Our specific samples demonstrate low reflectivity (< -10 dB) across the entire C-band, while also offering four distinct states (two-bit) for the passband (reflection/transmission) wave in a narrow window around 6.25 GHz, including circular polarization control or complete blockage. We experimentally demonstrated the switching capability for both chirality and intensity of the passing band wave. These results are significant in expanding the application scenarios of rasorbers with more versatile polarization controllability.

1. INTRODUCTION

C-band (including 5G) is distinguished by its high speed, low latency, high reliability, and high communication density and is gaining significant attentions in military technologies [1], particularly in areas such as time-sensitive targeting, covert special operations, command and control [2], training [3], and logistics. Besides the wide coverage capabilities and cost-effective communication solutions, C-band satellite beams are resilient to weather disturbances, making them ideal for ensuring consistent service availability [4, 5]. To counteract the reconnaissance radar detection for military equipments working in this band, frequency-selective rasorbers (FSRs) [6–10] having transmission windows [7, 8] for external communication are highly desired in practice. Moreover, in wireless applications that require minimized mutual interference and coupling, as well as a low radar cross section (RCS), an FSR featuring a reflection window [9, 10] is integrated with antennas to facilitate RCS reduction. Considering various application scenarios, active components like varactors or pin diodes have been utilized to realize tunable [11–13] or switchable [14–18] transmission windows. More comprehensive functions can be achieved by combining them together, such as dual-mode FSR that can switch a tunable transmission window into a reflection window [19] or a broad absorption band [20]. Graphene can be integrated into an FSR to have a tunable transmission amplitude [21]. These FSRs mostly work for the incidence of linearly polarized (LP) waves. In practice, there is a possibility of polarization rotation, as well as movement of the antenna position (with respect to the source). Circularly polarized (CP) antennas are well suited for dealing with these complex situations, offering flexibility for robust wireless communication [22, 23]. Furthermore, certain receiver antennas are sensitive to left-handed circularly polarized (LCP) or right-handed circularly polarized

(RCP) waves, underscoring the importance of controlling the chirality of the electromagnetic wave to ensure compatibility with diverse systems [24].

Chiral windows in the FSR have the practical significance by transmitting the LCP or RCP wave and completely blocking the others with opposite handedness [25–27]. These chiral-sensitive planar devices can be engineered by arrays of artificial meta-atoms without mirror and inversion symmetries [28–31]. By incorporating tunable elements, such as phase-transition materials or pin diodes, their functionality can be further expanded to achieve more versatile wave control [32–34]. In this work, we present a microwave chiral rasorber having a reconfigurable reflection/transmission window in the C-band (4–8 GHz), which can transmit LCP or RCP wave or even completely block it by controlling the state of metamaterial comprising two-bit meta-atoms. We utilize a pair of PIN diodes in the meta-atoms to actively modulate symmetries, and thus, chiral responses by controlling the coupling of localized electromagnetic dipolar resonant modes. Experimentally, our rasorbers show a wideband reflectivity less than -10 dB from 3.7 to 8.8 GHz, and simultaneously possess a variable reflection window around 6.25 GHz by offering four different states, namely the LCP, RCP, LP wave or complete blocking. These results are of practical importance by providing comprehensive polarization manipulation capabilities for the conventional band control for microwave rasorbers.

This paper is organized as follows. Section 2 discusses the unit cell of the reflective/transmissive switchable chiral polarizer and the design algorithm exploiting Jones matrix. Section 3 describes the design method of the FSR implementing the equivalent circuit model (ECM) and then comparing with the full-wave simulation, followed by the analysis of reflective/transmissive switchable chiral rasorber. Section 4 focuses on the experimental setup and discussion of the measured results, and Section 5 provides the conclusive remark.

* Corresponding author: Yungui Ma (yungui@zju.edu.cn).

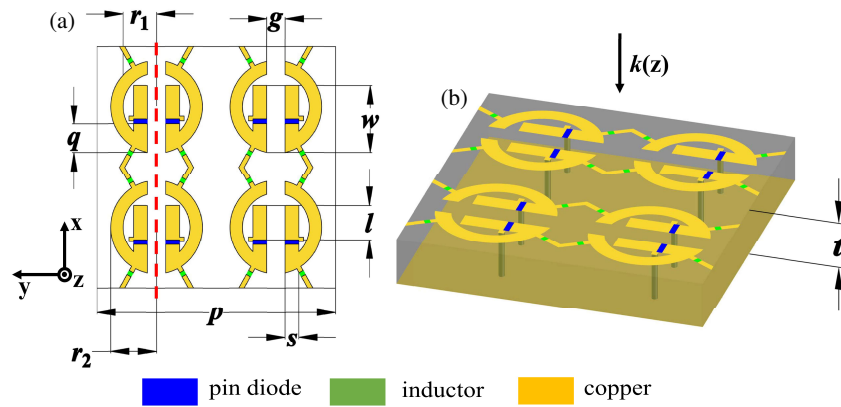


FIGURE 1. Unit-cell of the reflective switchable chiral polarizer; (a) top view, and (b) perspective view.

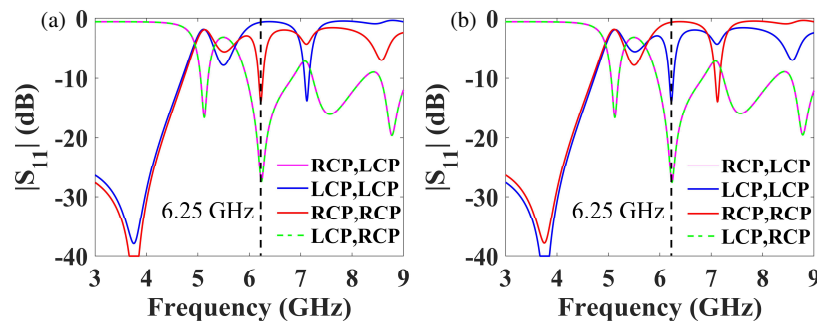


FIGURE 2. Simulated reflection for the reflective switchable chiral polarizer. (a) LCP polarizer: the pin diodes on the right side of the mirror-symmetry axis are under on-state, and (b) RCP polarizer: the pin diodes on the right side of the mirror-symmetry axis are under off-state.

2. REFLECTIVE/TRANSMISSIVE SWITCHABLE CHIRAL POLARIZER

2.1. Reflective Switchable Chiral Polarizer

The reconfigurable raserber is made of an FSR with a transmission window and a switchable chiral polarizer. Firstly, we design a reflective chiral polarizer with certain bandwidth in the C-band. Figs. 1(a) and (b) depict the schematic of four unit cells of the chiral polarizer design in the form of a metal-insulator-metal (MIM) configuration. The top metasurface is composed of metallic split-ring patterns, whose electromagnetic response could be freely modulated by the length of their arms and gap sizes. In order to gain different responses for the LCP and RCP waves (i.e., the chiral-sensitive behavior), the mirror symmetry of the unit cell needs to be violated, which is realized by using two pin diodes (blue color) embedded symmetrically in the two arms of meta-atoms. These lumped active elements act as a small resistor under forward bias voltage (on-state) or as a capacitor under zero bias voltage (off-state), corresponding to a short and open circuit, respectively [14–18]. When they work at different states, the unit symmetry breaks, and the chiral effect takes place. As such, the response for the LCP and RCP waves can be modulated or switched by dynamically controlling the bias states of the pair of pin diodes.

The CST Studio Suite software, along with its frequency-domain solver, is utilized to conduct full-wave simulations aiming to derive the scattering parameters of the device. In full-

wave simulation, pin diodes (SMP1330-040LF, Skyworks) are modeled by a circuit consisting of a 0.45 nH inductor in serial with a 1.5Ω resistor at the on-state or in serial with a 0.25 pF capacitor at the off-state. In this subsection, we design a switchable chiral polarizer to operate in the reflective mode with a copper substrate applied to block transmission. Firstly, we set the pin diode on the right side in one unit as on-state and the other on the left side as off-state. We introduce the inductor (LQW18AN15NG00D, 15 nH) to isolate the alternating current between the unit cells but to pass the direct current for biasing the pin diodes. The other ends of pin diodes are connected with the bottom ground through a conductive hole. We optimize the geometric parameters depicted in Fig. 1 as: $t = 3.5$ mm, $p = 26$ mm, $s = 1.5$ mm, $r_2 = 4.995$ mm, $r_1 = 3.64$ mm, $g = 2$ mm, $q = 3.046$ mm, $w = 7.219$ mm, and $l = 3.673$ mm. We use copper layers with conductivity $\sigma = 5.8 \times 10^7$ S/m and thickness 0.035 mm at the top and bottom, and FR4 with the relative permittivity of 4.2 and the loss tangent of 0.025 as spacer.

Herein, $r_{\text{LCP,LCP}}$ and $r_{\text{RCP,LCP}}$, respectively, denote the reflectivities of the LCP and RCP components under the LCP wave incidence, and $r_{\text{LCP,RCP}}$ and $r_{\text{RCP,RCP}}$ are those due to the RCP wave incidence. Furthermore, chiral polarization incident on a perfect electric conductor (PEC) reverses its handedness after reflection. The simulation results plotted in Fig. 2(a) indicate that, at the designed frequency of 6.25 GHz (middle region of the C-band), $r_{\text{LCP,RCP}}$, $r_{\text{RCP,RCP}}$, and $r_{\text{RCP,LCP}}$ are all smaller

than -10 dB, while $r_{\text{LCP,LCP}}$ is larger than -0.8 dB, thereby indicating the realization of the LCP polarizer operation. When the biasing states of the left and right pin diodes are switched, as shown in Fig. 2(b), the reflection features of the LCP and RCP incidences will be opposite to those shown in Fig. 2(a). Hence, a reflective switchable chiral polarizer is realized by controlling the operating state of pin diodes.

We apply Jones calculus to explain the chirality response of the above design. First, we define a transfer \hat{T} matrix to connect the complex amplitudes of the incident and transmitted fields [35], i.e.,

$$\begin{aligned} \begin{pmatrix} t_x \\ t_y \end{pmatrix} &= \begin{pmatrix} T_{xx} & T_{xy} \\ T_{yx} & T_{yy} \end{pmatrix} \begin{pmatrix} i_x \\ i_y \end{pmatrix} \\ &= \begin{pmatrix} A & B \\ C & D \end{pmatrix} \begin{pmatrix} i_x \\ i_y \end{pmatrix} = \widehat{T}_f \begin{pmatrix} i_x \\ i_y \end{pmatrix}, \end{aligned} \quad (1)$$

where the subscript f designates propagation in the forward direction (the positive z -axis shown in Fig. 1). In (2), \widehat{T}_b describes the transmission matrix for the wave propagating in the backward direction:

$$\widehat{T}_b = \begin{pmatrix} A & -C \\ -B & D \end{pmatrix}. \quad (2)$$

Changing the coordinate from the Cartesian base to the circular base, the \widehat{T}_f matrix becomes

$$\begin{aligned} \widehat{T}_f^{\text{circ}} &= \frac{1}{2} \begin{pmatrix} 1 & 1 \\ j & -j \end{pmatrix}^{-1} \widehat{T}_f \begin{pmatrix} 1 & 1 \\ j & -j \end{pmatrix} \\ &= \frac{1}{2} \begin{pmatrix} A+D+j(B-C) & A-D-j(B+C) \\ A-D+j(B+C) & A+D-j(B-C) \end{pmatrix}. \end{aligned} \quad (3)$$

If the unit cell is mirror-symmetric with respect to the xz -plane, the \widehat{T}_f matrix for the mirror image is identical to the original one, i.e.,

$$\begin{aligned} \begin{pmatrix} 1 & 0 \\ 0 & -1 \end{pmatrix}^{-1} \widehat{T}_f \begin{pmatrix} 1 & 0 \\ 0 & -1 \end{pmatrix} &= \widehat{T}_f \\ \rightarrow \begin{pmatrix} A & -B \\ -C & D \end{pmatrix} &= \begin{pmatrix} A & B \\ C & D \end{pmatrix} \rightarrow B = C = 0. \end{aligned} \quad (4)$$

If the unit cell is mirror-symmetric with respect to the yz -plane, the following equations can be obtained:

$$\begin{aligned} \begin{pmatrix} -1 & 0 \\ 0 & 1 \end{pmatrix}^{-1} \widehat{T}_f \begin{pmatrix} -1 & 0 \\ 0 & 1 \end{pmatrix} &= \widehat{T}_f \\ \rightarrow \begin{pmatrix} A & -B \\ -C & D \end{pmatrix} &= \begin{pmatrix} A & B \\ C & D \end{pmatrix} \rightarrow B = C = 0. \end{aligned} \quad (5)$$

From (4) and (5), the \widehat{T}_f matrix under circular base can be written as

$$\widehat{T}_f^{\text{circ}} = \frac{1}{2} \begin{pmatrix} A+D & A-D \\ A-D & A+D \end{pmatrix}, \quad (6)$$

which means that a chiral polarizer cannot be achieved as neither of the four elements of the matrix is unique. Hence, mirror-symmetry with respect to the plane parallel to the propagation axis should be broken for a chiral polarizer. Considering the structure in Fig. 1(a), its mirror structure with respect to the xz -plane (described by the red dashed line) is identical viewed from the back side. Thus, the following equations can be obtained:

$$\begin{aligned} \begin{pmatrix} 1 & 0 \\ 0 & -1 \end{pmatrix}^{-1} \widehat{T}_f \begin{pmatrix} 1 & 0 \\ 0 & -1 \end{pmatrix} &= \widehat{T}_b \\ \rightarrow \begin{pmatrix} A & -B \\ -C & D \end{pmatrix} &= \begin{pmatrix} A & -C \\ -B & D \end{pmatrix} \rightarrow B = C. \end{aligned} \quad (7)$$

Then, the \widehat{T}_f matrix under the circular base can be written as

$$\widehat{T}_f^{\text{circ}} = \frac{1}{2} \begin{pmatrix} A+D & A-D-2jB \\ A-D+2jB & A+D \end{pmatrix}. \quad (8)$$

In this case, if $A = 0.5$, $B = 0.5j$, and $D = -0.5$, the matrix under circular base turns into $\begin{pmatrix} 0 & 1 \\ 0 & 0 \end{pmatrix}$, realizing a chiral polarizer.

For the reflective device describing in Fig. 1, the Jones matrix under circular base should be written as

$$\begin{aligned} \widehat{R}^{\text{circ}} &= \frac{1}{2} \begin{pmatrix} A+D & A-D-2jB \\ A-D+2jB & A+D \end{pmatrix} \\ &= \begin{pmatrix} r_{\text{RCP,LCP}} & r_{\text{LCP,LCP}} \\ r_{\text{RCP,RCP}} & r_{\text{LCP,RCP}} \end{pmatrix}, \end{aligned} \quad (9)$$

Then, $r_{\text{RCP,LCP}} = r_{\text{LCP,RCP}}$ is satisfied. When the structure turns into its mirror image, substituting $-B$ for B into (9), the reflective matrix is written as

$$\begin{aligned} \widehat{R}^{\text{circ}} &= \frac{1}{2} \begin{pmatrix} A+D & A-D+2jB \\ A-D-2jB & A+D \end{pmatrix} \\ &= \begin{pmatrix} r_{\text{RCP,LCP}} & r_{\text{LCP,LCP}} \\ r_{\text{RCP,RCP}} & r_{\text{LCP,RCP}} \end{pmatrix}. \end{aligned} \quad (10)$$

It can be obtained from (9) and (10) that two mirrored structures interact with the LCP and RCP waves oppositely, which is confirmed by the simulation results shown in Fig. 2.

The underlying physical mechanism for the different helicity responses of mirror-asymmetric structures can be intuitively understood from the surface current distributions [33,34]. Fig. 3(a) depicts the current profile on the copper patterns of the LCP polarizer under the incidences of LCP and RCP waves. We see that the local inductive and capacitive responses of meta-atoms induce strong resonance at 6.25 GHz and greatly enhances the wave-matter interaction, and thus, the transfer efficiency for the polarizations [36]. Under the LCP incidence, the left and right copper arms of the unit cell exhibit identical instantaneous current directions, thereby determining weak dipolar response. However, under the RCP incidence, a closed

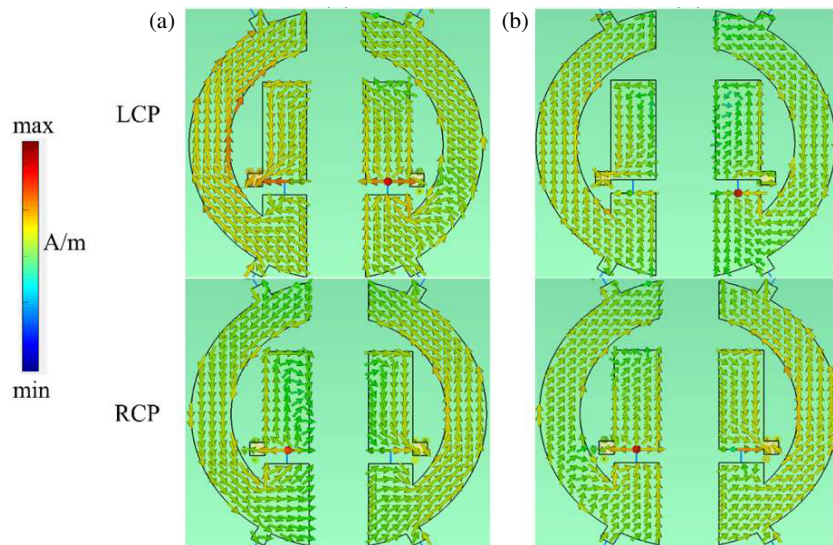


FIGURE 3. Simulated surface current distributions of the (a) LCP polarizer (left column), and (b) RCP polarizer (right column) under the LCP (top row) and RCP (lower row) incidences at 6.25 GHz.

current loop is formed by the two copper arms which leads to a local magnetic mode arising from the electric-magnetic dipolar coupling. The reflection waves from the magnetic resonance will destructively interfere with that directly reflected by the background, thus leading to perfect absorption at the designed frequencies for the RCP incidence [37], while the LCP wave is largely reflected. In the case of the RCP polarizer, illustrated in Fig. 3(b), the surface current patterns observed under the LCP and RCP incidences are analogous to those exhibited by the LCP polarizer under the RCP and LCP incidences, respectively. The surface current distributions of the LCP and RCP polarizer agree with their chirality-selective responses.

2.2. Transmissive Switchable Chiral Polarizer

We also design a switchable chiral polarizer to operate in the transmissive mode. The top layer has a similar layout to that in Fig. 1, and the copper substrate is replaced by the mirror structure of the upper layer, as Fig. 4 shows. We choose the geometric parameters to be: $t = 4.5$ mm, $p = 26$ mm, $s = 2.14$ mm, $r_2 = 4.803$ mm, $r_1 = 4.113$ mm, $g = 1.74$ mm,

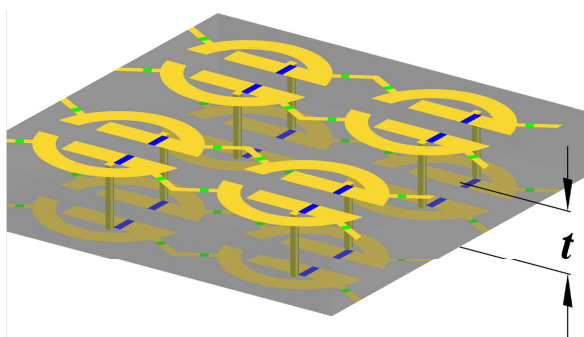


FIGURE 4. Perspective view of the unit cell of the transmissive switchable chiral polarizer.

$q = 2.961$ mm, $w = 4.338$ mm and $l = 0.877$ mm. We denote the transmissivity of the LCP and RCP components under the LCP wave incidence by $t_{LCP,LCP}$ and $t_{RCP,LCP}$, respectively, and those under the RCP wave incidence by $t_{LCP,RCP}$ and $t_{RCP,RCP}$, respectively.

The simulation results depicted in Figs. 5(a) and (b) indicate that at 6.25 GHz, the amplitudes of all reflective components are smaller than -10 dB. Additionally, $t_{RCP,LCP}$, $t_{LCP,RCP}$ and $t_{RCP,RCP}$ also exhibit values smaller than -10 dB, while $t_{LCP,LCP}$ exceeds -1.5 dB. This suggests the achievement of a transmissive chiral polarizer. By switching the pin diodes on both layers, and the simulation results plotted in Figs. 5(c) and (d) show that the mirror structure interacts with the LCP wave in a manner similar to the previous structure's interaction with the RCP wave. Consequently, control of the operation of pin diodes yields a switchable transmissive chiral polarizer.

Here, we also apply Jones matrix to reveal the condition for a transmissive switchable chiral polarizer. In order to speed up the optimization process, we choose the bottom layer as the mirror image of the top layer with respect to the xz -plane, reducing the number of variable geometric parameters. In this scenario, the structure remains unchanged when being viewed from the back side, which is in contrast to the reflective design where the mirror image with respect to the xz -plane is the same (upon viewing from the back side). It should be noted that, if the bottom layer is identical to the top layer, a transmissive chiral polarizer can also be achieved by designing appropriate geometric parameters, as discussed in the previous subsection. Subsequently, considering the structure depicted in Fig. 4, alternative equations distinct from those presented in the preceding subsection can be derived:

$$\widehat{T}_f = \widehat{T}_b \rightarrow \begin{pmatrix} A & B \\ C & D \end{pmatrix} = \begin{pmatrix} A & -C \\ -B & D \end{pmatrix} \rightarrow B = -C, \quad (11)$$

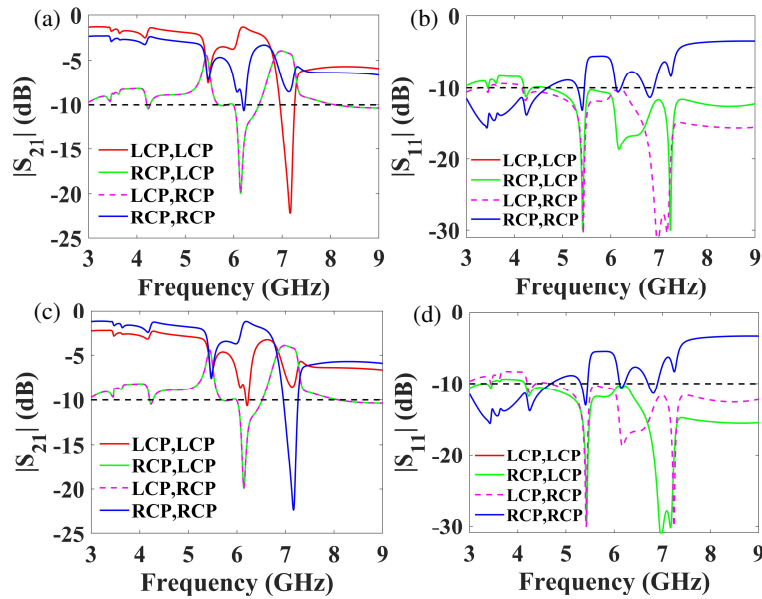


FIGURE 5. Simulated S -parameters for the transmissive switchable chiral polarizer. (a) & (b) LCP polarizer: the pin diodes of the upper layer on the right side of the mirror-symmetry axis are under on-state, and (c) & (d) RCP polarizer: the pin diodes of the upper layer on the right side of the mirror-symmetry axis are under off-state.

The \hat{T}_f matrix under the circular base can then be written as

$$\begin{aligned} \widehat{T}^{circ} &= \frac{1}{2} \begin{pmatrix} A + D + 2jB & A - D \\ A - D & A + D - 2jB \end{pmatrix} \\ &= \begin{pmatrix} t_{LCP,LCP} & t_{RCP,LCP} \\ t_{LCP,RCP} & t_{RCP,RCP} \end{pmatrix}, \end{aligned} \quad (12)$$

and the reflective matrix (under the circular base) will be

$$\begin{aligned} \widehat{R}^{circ} &= \frac{1}{2} \begin{pmatrix} A + D + 2jB & A - D \\ A - D & A + D - 2jB \end{pmatrix} \\ &= \begin{pmatrix} r_{RCP,LCP} & r_{LCP,LCP} \\ r_{RCP,RCP} & r_{LCP,RCP} \end{pmatrix}, \end{aligned} \quad (13)$$

We then obtain $t_{RCP,LCP} = t_{LCP,RCP}$, $r_{LCP,LCP} = r_{RCP,RCP}$. When the structure turns into its mirror image, substituting $-B$ for B into (12) and (13), the transmissive and reflective matrices can be written as

$$\begin{aligned} \widehat{T}^{circ} &= \frac{1}{2} \begin{pmatrix} A + D - 2jB & A - D \\ A - D & A + D + 2jB \end{pmatrix} \\ &= \begin{pmatrix} t_{LCP,LCP} & t_{RCP,LCP} \\ t_{LCP,RCP} & t_{RCP,RCP} \end{pmatrix}, \end{aligned} \quad (14)$$

and

$$\begin{aligned} \widehat{R}^{circ} &= \frac{1}{2} \begin{pmatrix} A + D - 2jB & A - D \\ A - D & A + D + 2jB \end{pmatrix} \\ &= \begin{pmatrix} r_{RCP,LCP} & r_{LCP,LCP} \\ r_{RCP,RCP} & r_{LCP,RCP} \end{pmatrix}, \end{aligned} \quad (15)$$

respectively. Therefore, we can obtain from (14) and (15) that two mirror-structures interact with the LCP and RCP waves oppositely in both the transmissive and reflective modes, which is confirmed by the simulation results shown in Fig. 5.

3. REFLECTIVE/TRANSMISSIVE SWITCHABLE CHIRAL RASORBER

The aforementioned discussion focused on the concept of transmissive and reflective chiral polarizers operating at 6.25 GHz. However, in practical applications, the incident microwave signal may be broadband in the C-band. In cases where only a narrow-band wave near 6.25 GHz is required, and low reflectivity in the C-band is necessary for reflective mode, as well as low reflectivity and transmissivity (in the C-band) for transmissive mode, we propose an FSR to address these requirements. Fig. 6(d) depicts the unit cell of reflective switchable chiral rasorber consisting of three layers, namely the absorptive (Fig. 6(a)), bandpass (Fig. 6(b)), and chiral layers. We design these layers to have the same window at 6.25 GHz, with the resistors (on the absorptive layer) absorbing the incident wave at other frequencies in the C-band. The absorptive and bandpass layers collectively function as an FSR with low reflectivity in the C-band; the working mechanism can be explained using the transmission-line theory [38, 39].

In order to determine the suitable parameter for the FSR, an ECM is utilized as a design approach, as illustrated in Fig. 6(c). The design incorporates the consideration of free-space wave impedance (Z_0), with the band-pass layer being conceptualized as a parallel circuit. The components within the model include a slot, an outer patch, and an inner square loop, which are, respectively, denoted as capacitor C_{02} , inductor L_{22} , and L_{21} . Here L_{22} serves the purpose of establishing a parallel

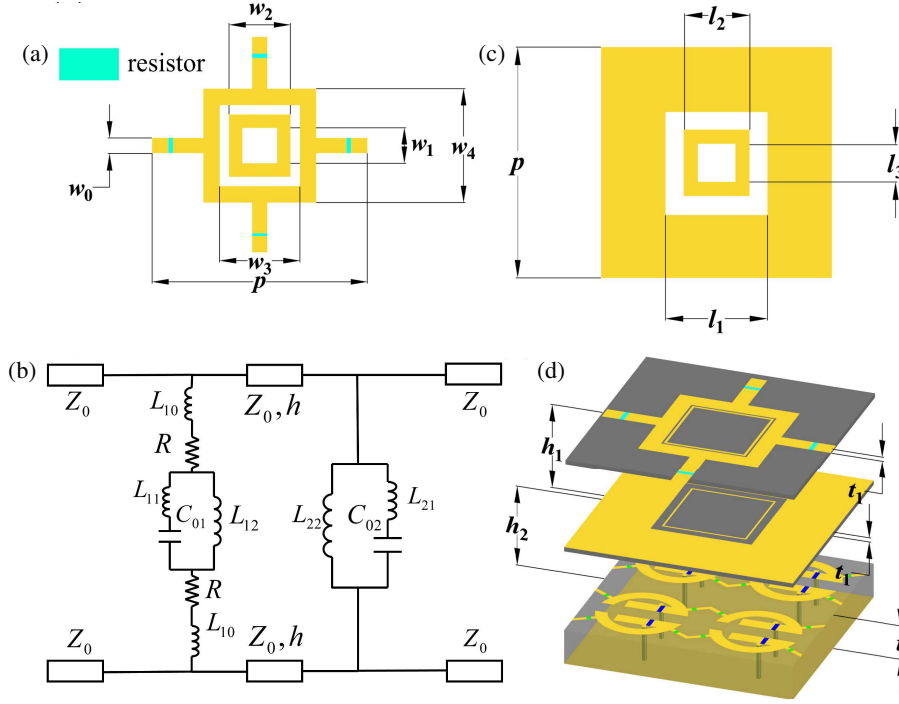


FIGURE 6. Unit cell of the reflective switchable chiral rasorber. (a) Top view of the absorptive layer. (b) Top view of the bandpass layer. (c) ECM of the proposed FSR. (d) Perspective view of the reflective switchable chiral rasorber.

$$S_{11} = \frac{Y_2 Z_0 (-\cos \theta + j \sin \theta) - Y_1 Z_0 (\cos \theta + j \sin \theta) - j Z_0^2 Y_1 Y_2 \sin \theta}{[(Y_1 + Y_2) Z_0 + 2](\cos \theta + j \sin \theta) + j Z_0^2 Y_1 Y_2 \sin \theta}, \quad (16)$$

$$S_{21} = \frac{2}{[(Y_1 + Y_2) Z_0 + 2](\cos \theta + j \sin \theta) + j Z_0^2 Y_1 Y_2 \sin \theta},$$

where Y_1 and Y_2 are, respectively, the admittances of the absorptive and band-pass layers, $\theta = 2\pi f h/c$, and f and c , respectively, denote the frequency and speed of wave in free-space. When a transmission window is needed, $Y_1 = Y_2 = 0$, i.e., the impedance of the two layers equals infinity at the same frequency. So, to achieve the transmission window, the ECM in Fig. 6(c) is applied, according to which, the expressions for Y_1 and Y_2 can be written as

$$Y_1 = \frac{1}{2(j\omega L_{10} + R) + \frac{1}{\frac{1}{j\omega L_{12}} + \frac{1}{j\omega L_{11}} + \frac{1}{j\omega C_{01}}}}, \quad (17)$$

$$Y_2 = \frac{1}{j\omega L_{22}} + \frac{1}{j\omega L_{21} + \frac{1}{j\omega C_{02}}},$$

where $\omega = 2\pi f$. From the above equations, the frequencies of transmission window of the two ECM layers can be expressed as

$$f_1 = \frac{\sqrt{\frac{1}{(L_{11} + L_{12})C_{01}}}}{2\pi} = \frac{\sqrt{\frac{1}{(L_{21} + L_{22})C_{02}}}}{2\pi}. \quad (18)$$

As the condition of equal frequency (i.e., $f_1 = f_2 = f_0$) is needed to achieve a transmission window, the relationship of

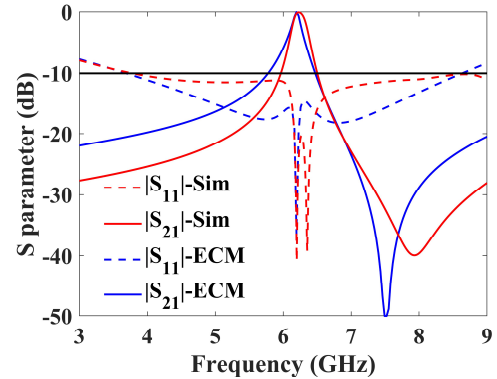


FIGURE 7. Comparison of the S -parameters of the FSR obtained using the ECM and full-wave simulation.

LCR parameters can be written as

$$(L_{11} + L_{12})C_{01} = (L_{21} + L_{22})C_{02} = 1/(2\pi f_0)^2. \quad (19)$$

The S -parameters can be derived from Equations (19), (17), and (16). Our objective is to ensure that $|S_{11}|$ remains below -10 dB within the frequency range of 4–8 GHz. To achieve this, particle swarm optimization toolbox in Matlab is employed, with the design frequency fixed at 6.25 GHz and the

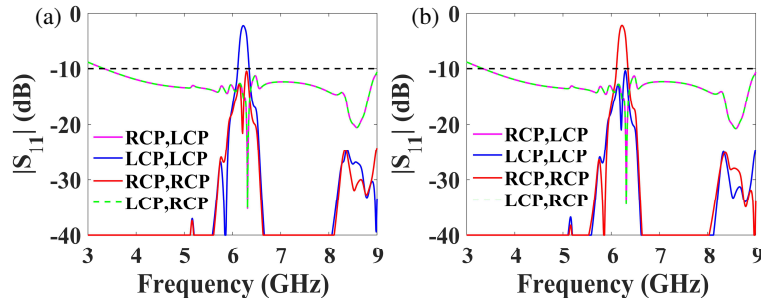


FIGURE 8. Simulated reflection for the reflective switchable chiral rasorber. The reflectivity (a) with the right (left) side pin diode in one unit cell under the on- (off-) state, and (b) with the reverse states for the pin diodes.

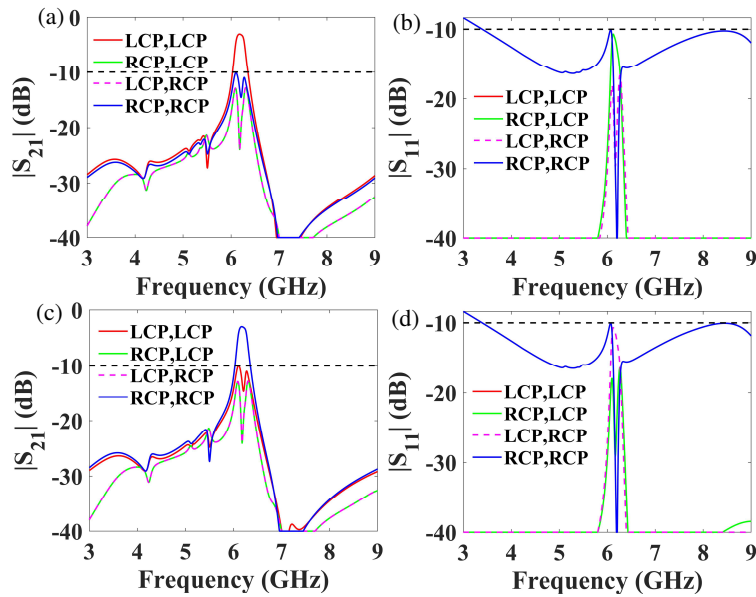


FIGURE 9. Simulated S -parameters for the transmissive switchable chiral rasorber. The S -parameters (a) & (b) with the right (left) side pin diode in one unit cell of the top layer under on- (off-) state, and (c) & (d) with the reverse states for the pin diodes.

parameters C_{02} , L_{22} , L_{21} , L_{10} , R , C_{01} , L_{11} , and L_{12} designated as variables. Through a series of iterative processes, the results progressively converge towards the desired target, ultimately yielding the parameters that satisfy our objective. Once we obtain the total parameters of the ECM, we design the geometric parameters of the real structure (Fig. 6) to match the LCR parameters. Fig. 7 presents a comparison of the S -parameters calculated from the full-wave simulation (F4B with permittivity $\varepsilon = 2.65$ is used as substrates, and the thickness of copper is 0.018 mm) and the ECM calculation with the specified parameters: $t_1 = 0.5$ mm, $h_1 = 12.5$ mm, $p = 26$ mm, $l_1 = 11.2$ mm, $l_2 = 10.2$ mm, $l_3 = 8.2$ mm, $w_0 = 1.8$ mm, $w_1 = 8.75$ mm, $w_2 = 9.3$ mm, $w_3 = 9.7$ mm, $w_4 = 13.6$ mm, $C_{02} = 0.1568$ pF, $L_{22} = 2.863$ nH, $L_{21} = 1.34$ nH, $L_{10} = 0.1$ nH, $R = 160$ Ω , $C_{01} = 0.1334$ pF, $L_{11} = 1$ nH, and $L_{12} = 3.203$ nH. The resonant frequencies determined through the full-wave simulation and ECM calculation demonstrate a similarity. However, minor deviations exist, as the ECM calculations rely on fixed LCR parameters and do not consider the actual electric current distributions affected by electromag-

netic coupling within the geometric structure that determines S -parameters.

We simulate the unit cell in Fig. 6(d) with $h_2 = 6$ mm to obtain the S -parameters. The results depicted in Fig. 8(a) indicate that a reflective chiral rasorber with $r_{LCP,RCP}$, $r_{RCP,RCP}$, and $r_{RCP,LCP}$ below -10 dB across the whole C-band is obtained. At the same time, $r_{LCP,LCP}$ is larger than -1.8 dB at 6.25 GHz. Moreover, when the structure turns into its mirror image with respect to the xz -plane, the simulation results plotted in Fig. 8(b) demonstrate switchability between the reflective LCP and RCP rasorbers. We design the transmissive rasorber by replacing the chiral layer in Fig. 6 with that drawn in Fig. 4 and replacing the substrates of the absorptive and band-pass layers with Rogers 4003 (permittivity $\varepsilon = 3.55$) with the specified parameters: $t_1 = 0.5$ mm, $h_1 = 12.5$ mm, $h_2 = 6.5$ mm, $p = 26$ mm, $l_1 = 12$ mm, $l_2 = 8.95$ mm, $l_3 = 8.55$ mm, $w_0 = 1$ mm, $w_1 = 7.95$ mm, $w_2 = 8.55$ mm, $w_3 = 9.4$ mm, and $w_4 = 13$ mm. The findings depicted in Figs. 9(a) and (b) indicate successful realization of a transmissive chiral rasorber with reflectivity below -10 dB across the entire C-band. Addi-

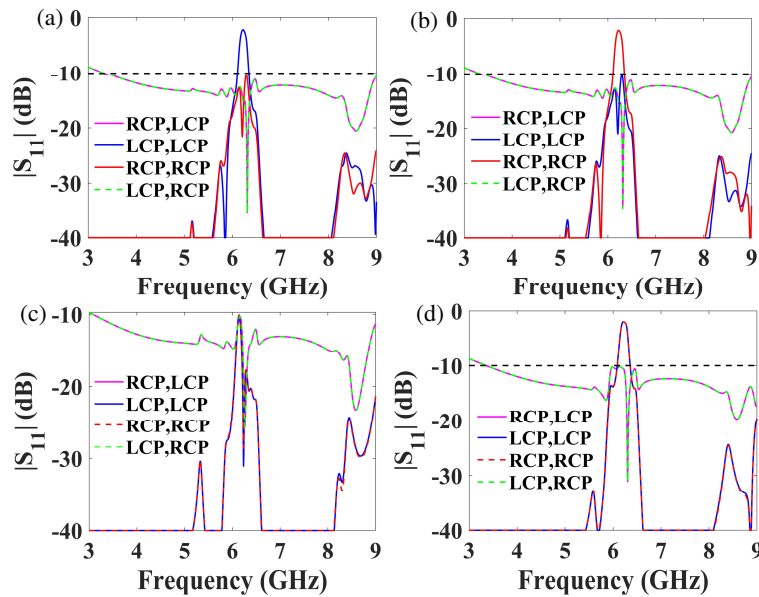


FIGURE 10. Simulated results under four states of the reflective switchable chiral rasorber. (a) LCP rasorber: the reflectivity when pin diodes on the right side of the mirror-symmetry axis are under on-state. (b) RCP rasorber: the reflectivity when pin diodes on the right side of the mirror-symmetry axis are under off-state. (c) Absorber: the reflectivity when pin diodes are all under off-state. (d) Rasorber: the reflectivity when pin diodes are all under on-state.

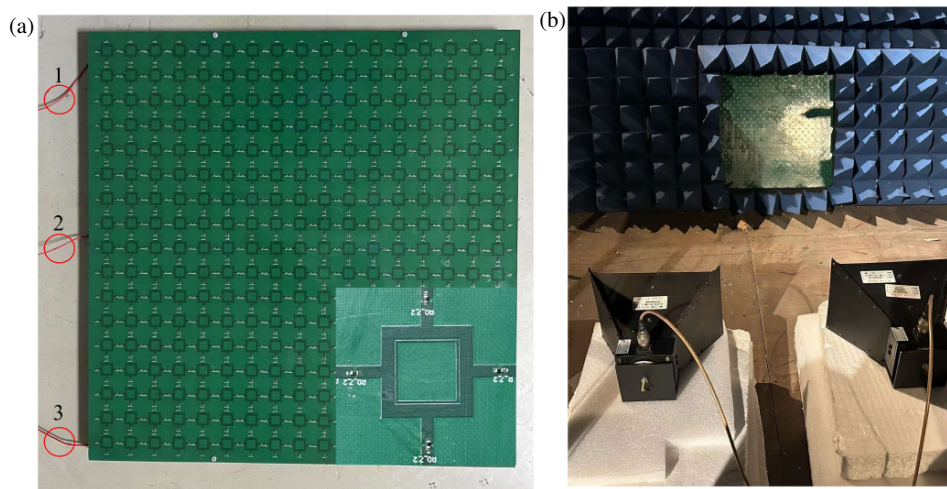


FIGURE 11. Experimental setup of the free-space measurement. (a) Sample of the reflective switchable chiral rasorber (a zoom version of the unit cell is positioned in the lower right corner), and (b) configuration of the setup.

tionally, $t_{RCP,LCP}$, $t_{LCP,RCP}$, and $t_{RCP,RCP}$ are all below -10 dB, while $t_{LCP,LCP}$ is greater than -3 dB at 6.25 GHz. Furthermore, the simulation results in Figs. 9(c) and (d) demonstrate the attainment of a switchable function between the transmissive LCP and RCP rasorbers when the structure undergoes a mirror image transformation with respect to the xz -plane.

4. EXPERIMENTAL RESULTS AND DISCUSSIONS ON THE REFLECTIVE SWITCHABLE CHIRAL RASORBER

To verify the performance of the switchable chiral rasorber, we study the reflective device experimentally. We use two

foam spacers with the relative permittivity of 1.1 to replace the air spacer for the purpose of ensuring flatness of the device. Fig. 10 depicts the simulation results with the parameters: $t_1 = 0.5$ mm, $h_1 = 13$ mm, $h_2 = 5.7$ mm, $p = 26$ mm, $l_1 = 11.578$ mm, $l_2 = 9.434$ mm, $l_3 = 9.065$ mm, $w_0 = 1.984$ mm, $w_1 = 8.889$ mm, $w_2 = 9.364$ mm, $w_3 = 9.682$ mm, and $w_4 = 12.836$ mm. The implemented design serves as a two-bit switchable metamaterial, which has four switchable operating states across the C-band, namely the LCP rasorber, RCP rasorber, absorber, and rasorber. If the pin diodes on the left side of the mirror-symmetry axis are under on-state and those on the right side under off-state, we obtain an LCP rasorber. If

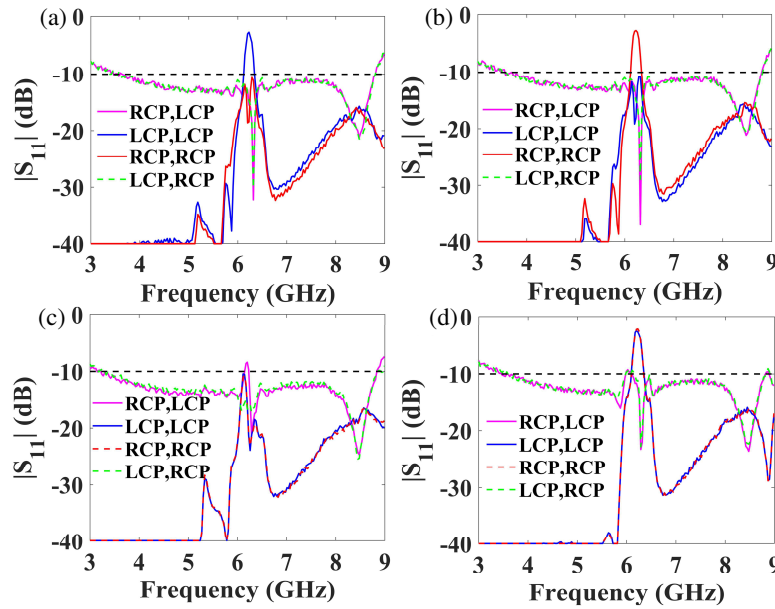


FIGURE 12. Measured reflection under four states of the reflective switchable chiral rasorber. (a) LCP rasorber: line 1 is connected to the anode of DC source with 0.4 V biased voltage. (b) RCP rasorber: line 3 is connected to the anode of DC source with 0.4 V biased voltage. (c) Absorber: all lines are not connected to DC source. (d) Rasorber: line 1 and 3 are both connected to the anode of DC source with 0.4 V biased voltage.

the states of the pin diodes are reversed, a LCP rasorber will be transformed into a RCP rasorber. When all pin diodes are under off-state, a broadband absorber is realized, and under on-state, a circular-polarization-insensitive rasorber is achieved.

We fabricate a prototype consisting of 17×17 unit cells using printed circuit board (PCB) technology, as depicted in Fig. 11(a). Three bias lines labeled as 1, 2, and 3 are soldered to the bottom layer. Line 2 is linked to the ground copper plane, while lines 1 and 3 are connected to the upper interval columns. We utilize a DC voltage source to supply forward-current for the pin diodes, with line 2 being connected to the ground terminal of the source. Here, we assemble the multilayers together by plastic nylon screws and measure the S -parameters of the switchable chiral rasorber prototype in an anechoic chamber using the free-space method [13, 20], employing a Vector Network Analyzer (VNA, RS-ZVA40).

$$\begin{pmatrix} r_{\text{RCP,LCP}} & r_{\text{LCP,LCP}} \\ r_{\text{RCP,RCP}} & r_{\text{LCP,RCP}} \end{pmatrix} = \frac{1}{2} \begin{pmatrix} r_{xx} + r_{yy} + j(r_{xy} - r_{yx}) & r_{xx} - r_{yy} + j(r_{xy} + r_{yx}) \\ r_{xx} - r_{yy} - j(r_{xy} + r_{yx}) & r_{xx} + r_{yy} - j(r_{xy} - r_{yx}) \end{pmatrix}. \quad (20)$$

The experimental results in Fig. 12 indicate the successful implementation of a reflective switchable absorber. Specifically, it is observed that $r_{\text{LCP,LCP}}$ exceeds -2.7 dB at 6.25 GHz when the bias line 1 is connected to the anode of the DC voltage source; $r_{\text{LCP,RCP}}$, $r_{\text{RCP,RCP}}$, and $r_{\text{RCP,LCP}}$ across the entire C-band remain below -10 dB. Conversely, when the anode of the DC voltage source is connected to the bias line 3, $r_{\text{RCP,RCP}}$ exceeds -2.6 dB at 6.25 GHz, while the other reflective components across the C-band remain below -10 dB. In the absence of a voltage source, a broadband absorber with all re-

As illustrated in Fig. 11(b), two horn antennas (functioning as the transmitter and receiver) operating in the 2–18 GHz band are connected to the VNA. The distance between the antennas and the prototype is larger than 1.5 m during the measurement. We place the prototype in the hole of an absorbing screen with its center being carefully aligned with that of the antenna apertures. The measured S -parameters for reflection are normalized by the reflection spectrum of a same-sized copper mirror placed at the same distance with the sample. Due to the constraints of the setup, there is a small incidence angle of $\sim 8^\circ$ in the measurement. To evaluate the performance of the rasorber under chiral incidence, we measure linear co-polarization (r_{xx} , r_{yy}) and cross-polarization (r_{xy} , r_{yx}) reflection coefficients. According to Equation (3), the reflection matrix under circular base can be processed as

fective components nearly below -10 dB is achieved. Furthermore, the reflectivity without polarization conversion exceeds -2.8 dB at 6.25 GHz when both the bias lines 1 and 3 are connected to the anode of the DC voltage source, while the reflectivity with polarization conversion across the entire C-band remains nearly below -10 dB. Overall, the experimental results agree well with those obtained by the full-wave simulation route. However, the recorded amplitudes of the reflection window for LCP, RCP, and polarization-insensitive rasorbers at 6.25 GHz exhibit lower values (-2.7 dB, -2.6 dB,

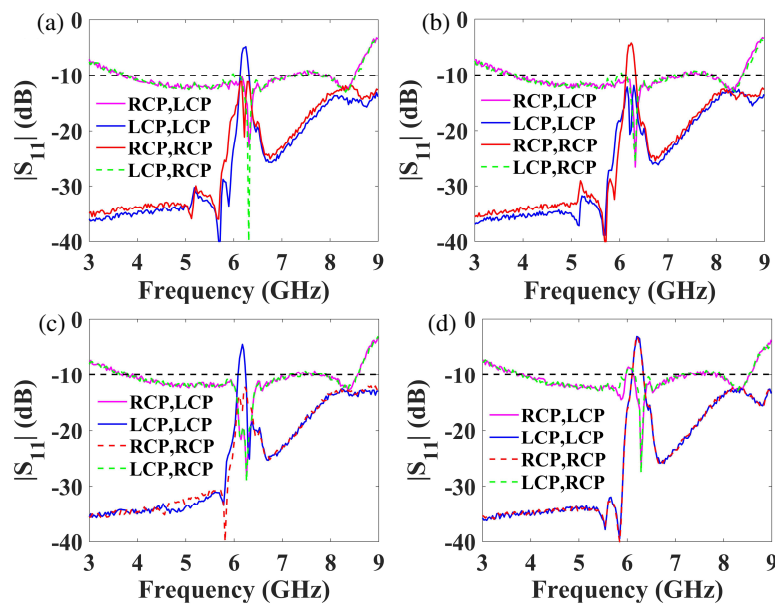


FIGURE 13. Measured reflection under 15° oblique incidence. (a) LCP rasorber. (b) RCP rasorber. (c) Absorber. (d) Rasorber.

TABLE 1. Comparison with other rasorbers.

Ref.	Amplitude of window	Reflection band below -10 dB	Polarization	Switchable	Bit
[6]	-0.73 dB	0.95–3.3 GHz	Linear & Single	No	0
[8]	-0.68 dB	2.5–6.79 GHz	Linear & Dual	No	0
[16]	-1.28 dB	1.79–5.25 GHz	Linear & Single	Yes	1
[18]	-1.7 dB	0.8–3.2 GHz	Linear & Dual	Yes	1
Our work	-2.7 dB	3.7–8.8 GHz	Chiral	Yes	2

and -2.8 dB, respectively) than the simulated values (above -2.2 dB). Additionally, the measured reflection of reflective components, intended to be below -10 dB, is inferior to the simulation values when the device operates as a C-band absorber or common rasorber, thereby slightly disrupting the broadband reflection below -10 dB. These minor discrepancies in the reflection profiles are primarily attributed to the deviation from normal incidence in the experimental setup.

To explore the impact of oblique incidence, we measured the frequency responses of the device at incident angles of 15° . The results presented in Fig. 13 demonstrate a decline in performance as the incident angle surpasses 15° , characterized by a decrease in the amplitude of the transmission window and a reduction in the low reflection bandwidth. Specifically, at an incident angle of 15° , the amplitudes of the reflection window for LCP, RCP, and polarization-insensitive absorbers at 6.25 GHz exhibit values below -4 dB. Moreover, the broadband reflectivity below -10 dB is not met near 6.25 GHz and 8 GHz.

The comparisons of the performance between our design and other previously published rasorbers are listed in Table 1. These rasorbers are proposed to work under linear polarization (single linear polarization or dual linear polarization) with or without the function to switch on/off the transmission window. However, they cannot switch the orthogonal polarization of output electromagnetic wave. It is seen that our design which expands

the type of linear rasorbers has the advantages of two-bit configurable functions and chiral-polarization control capability. However, it should be noted that, compared to FSRs with nearly perfect transmission window designed for linear polarization incidence, the reflection/transmission windows implemented in this work have a relatively larger insertion loss due to the resonance attenuation caused by the meta-atoms which are necessary to absorb one of the CP waves. The issue may be released if the mirror reflection of the unwanted circular polarization is suppressed by a random scattering rather than a total absorption [40]. In addition, the rasorber designed in this work features a 3 dB bandwidth of ~ 0.2 GHz, which is narrower than the FSRs operated in linear polarizations [8, 12, 13]. This narrower bandwidth is a consequence of the transmission window of the FSR to achieve low reflectivity across the C-band. As the transmission window of the FSR widens, the reflection of other reflective components near the chiral window (6.25 GHz) will exceed -10 dB, leading to stringent requirements on the incident angle.

5. CONCLUSION

The afore-discussed results determine that a reflective/transmissive two-bit microwave chiral rasorber is capable of switching its reflective/transmissive window be-

tween the LCP and RCP waves through the use of pin diodes; the sensitivity to chirality is realized by mirror-asymmetric structures. Experimental results indicate the reflective functional device being switchable among four different states, namely LCP rasorber, RCP rasorber, broadband absorber, and polarization-insensitive rasorber. The reflectivity of undesirable polarization components remains below -10 dB in the entire C-band, thereby determining device to be promising as a C-band chiral rasorber to transmit the LCP or RCP wave with a certain bandwidth — the feature crucial in CP wave communication systems. It may also be employed in chiral sensing to probe the amplitude of the LCP and/or RCP waves [41, 42].

ACKNOWLEDGEMENT

This work is supported in part by the National Natural Science Foundation of China under Grant 62075196, in part by the Natural Science Foundation of Zhejiang Province under Grant LXZ22F050001 and Grant LDT23F05014F05, in part by the Leading Innovative and Entrepreneur Team Introduction Program of Zhejiang under Grant 2021R01001, and in part by the Fundamental Research Funds for the Central University under Grant 2021FZZX001-07.

REFERENCES

- [1] Bajracharya, R., R. Shrestha, S. A. Hassan, H. Jung, and H. Shin, "5G and beyond private military communication: Trend, requirements, challenges and enablers," *IEEE Access*, Vol. 11, 83 996–84 012, 2023.
- [2] Brown, P. N., H. P. Borowski, and J. R. Marden, "Security against impersonation attacks in distributed systems," *IEEE Transactions on Control of Network Systems*, Vol. 6, No. 1, 440–450, Mar. 2019.
- [3] Shrestha, R., A. Omidkar, S. A. Roudi, R. Abbas, and S. Kim, "Machine-learning-enabled intrusion detection system for cellular connected UAV networks," *Electronics*, Vol. 10, No. 13, 1549, Jul. 2021.
- [4] Lagunas, E., C. G. Tsinos, S. K. Sharma, and S. Chatzinotas, "5G cellular and fixed satellite service spectrum coexistence in C-band," *IEEE Access*, Vol. 8, 72 078–72 094, 2020.
- [5] Irsigler, M., G. W. Hein, and A. Schmitz-Peiffer, "Use of C-band frequencies for satellite navigation: Benefits and drawbacks," *GPS Solutions*, Vol. 8, 119–139, 2004.
- [6] Shen, Z., J. Wang, and B. Li, "3-D frequency selective rasorber: Concept, analysis, and design," *IEEE Transactions on Microwave Theory and Techniques*, Vol. 64, No. 10, 3087–3096, Oct. 2016.
- [7] Chen, Q., D. Sang, M. Guo, and Y. Fu, "Frequency-selective rasorber with interabsorption band transparent window and interdigital resonator," *IEEE Transactions on Antennas and Propagation*, Vol. 66, No. 8, 4105–4114, Aug. 2018.
- [8] Shang, Y., Z. Shen, and S. Xiao, "Frequency-selective rasorber based on square-loop and cross-dipole arrays," *IEEE Transactions on Antennas and Propagation*, Vol. 62, No. 11, 5581–5589, Nov. 2014.
- [9] Mei, P., X. Q. Lin, J. W. Yu, A. Boukarkar, P. C. Zhang, and Z. Q. Yang, "Development of a low radar cross section antenna with band-notched absorber," *IEEE Transactions on Antennas and Propagation*, Vol. 66, No. 2, 582–589, Feb. 2018.
- [10] Mei, P., X. Q. Lin, J. W. Yu, and P. C. Zhang, "A band-notched absorber designed with high notch-band-edge selectivity," *IEEE Transactions on Antennas and Propagation*, Vol. 65, No. 7, 3560–3567, Jul. 2017.
- [11] Guo, Q., Q. Chen, J. Su, and Z. Li, "A varactor-tunable rasorber using tripole and ring slot elements," *International Journal of Antennas and Propagation*, Vol. 2021, No. 1, 9766379, Dec. 2021.
- [12] Wang, Y., S.-S. Qi, Z. Shen, and W. Wu, "Tunable frequency-selective rasorber based on varactor-embedded square-loop array," *IEEE Access*, Vol. 7, 115 552–115 559, 2019.
- [13] Wu, L., S. Zhong, J. Huang, and T. Liu, "Broadband frequency-selective rasorber with varactor-tunable interabsorption band transmission window," *IEEE Transactions on Antennas and Propagation*, Vol. 67, No. 9, 6039–6050, Sep. 2019.
- [14] Bakshi, S. C., D. Mitra, and S. Ghosh, "A frequency selective surface based reconfigurable rasorber with switchable transmission/reflection band," *IEEE Antennas and Wireless Propagation Letters*, Vol. 18, No. 1, 29–33, Jan. 2019.
- [15] Bakshi, S. C., D. Mitra, and F. L. Teixeira, "Wide-angle broadband rasorber for switchable and conformal application," *IEEE Transactions on Microwave Theory and Techniques*, Vol. 69, No. 2, 1205–1216, Feb. 2021.
- [16] Han, Y., W. Che, X. Xiu, W. Yang, and C. Christopoulos, "Switchable low-profile broadband frequency-selective rasorber/absorber based on slot arrays," *IEEE Transactions on Antennas and Propagation*, Vol. 65, No. 12, 6998–7008, Dec. 2017.
- [17] Li, R., J. Tian, B. Jiang, Z. Lin, B. Chen, and H. Hu, "A switchable frequency selective rasorber with wide passband," *IEEE Antennas and Wireless Propagation Letters*, Vol. 20, No. 8, 1567–1571, Aug. 2021.
- [18] Qian, G., J. Zhao, X. Ren, K. Chen, T. Jiang, Y. Feng, and Y. Liu, "Switchable broadband dual-polarized frequency-selective rasorber/absorber," *IEEE Antennas and Wireless Propagation Letters*, Vol. 18, No. 12, 2508–2512, Dec. 2019.
- [19] Bakshi, S. C., D. Mitra, and F. L. Teixeira, "Multifunctional frequency selective rasorber with dual mode and continuous tunability," *IEEE Transactions on Antennas and Propagation*, Vol. 69, No. 9, 5704–5715, Sep. 2021.
- [20] Phon, R., S. Ghosh, and S. Lim, "Active frequency selective surface to switch between absorption and transmission band with additional frequency tuning capability," *IEEE Transactions on Antennas and Propagation*, Vol. 67, No. 9, 6059–6067, Sep. 2019.
- [21] Xue, Z., S. Zhong, and Y. Ma, "Graphene-FSS hybrid absorptive structure with amplitude/frequency dual-modulated passband," *IEEE Antennas and Wireless Propagation Letters*, Vol. 20, No. 9, 1711–1715, Sep. 2021.
- [22] Ma, Y., J. Li, and R. Xu, "Design of an omnidirectional circularly polarized antenna," *IEEE Antennas and Wireless Propagation Letters*, Vol. 16, 226–229, 2017.
- [23] Rezaeieh, S. A., A. Abbosh, and M. A. Antoniadis, "Broadband planar circularly polarised antenna for ultra-high frequency applications," *IET Microwaves, Antennas & Propagation*, Vol. 8, No. 4, 263–271, Mar. 2014.
- [24] Zhao, S. and Y. Dong, "Circularly polarized beam-steering microstrip leaky-wave antenna based on coplanar polarizers," *IEEE Antennas and Wireless Propagation Letters*, Vol. 21, No. 11, 2259–2263, Nov. 2022.
- [25] Plum, E. and N. I. Zheludev, "Chiral mirrors," *Applied Physics Letters*, Vol. 106, No. 22, 221901, Jun. 2015.
- [26] Jing, L., Z. Wang, R. Maturi, B. Zheng, H. Wang, Y. Yang, L. Shen, R. Hao, W. Yin, E. Li, and H. Chen, "Gradient chi-

- ral metamirrors for spin-selective anomalous reflection,” *Laser & Photonics Reviews*, Vol. 11, No. 6, 1700115, Nov. 2017.
- [27] Wang, Z., H. Jia, K. Yao, W. Cai, H. Chen, and Y. Liu, “Circular dichroism metamirrors with near-perfect extinction,” *ACS Photonics*, Vol. 3, No. 11, 2096–2101, Sep. 2016.
- [28] Mun, J., M. Kim, Y. Yang, T. Badloe, J. Ni, Y. Chen, C.-W. Qiu, and J. Rho, “Electromagnetic chirality: From fundamentals to nontraditional chiroptical phenomena,” *Light: Science & Applications*, Vol. 9, No. 1, 139, 2020.
- [29] Gorkunov, M. V., A. A. Antonov, V. R. Tuz, A. S. Kupriianov, and Y. S. Kivshar, “Bound states in the continuum underpin near-lossless maximum chirality in dielectric metasurfaces,” *Advanced Optical Materials*, Vol. 9, No. 19, 2100797, Oct. 2021.
- [30] Chen, C., S. Gao, W. Song, H. Li, S.-N. Zhu, and T. Li, “Metasurfaces with planar chiral meta-atoms for spin light manipulation,” *Nano Letters*, Vol. 21, No. 4, 1815–1821, Feb. 2021.
- [31] Li, W., Z. J. Coppens, L. V. Besteiro, W. Wang, A. O. Govorov, and J. Valentine, “Circularly polarized light detection with hot electrons in chiral plasmonic metamaterials,” *Nature Communications*, Vol. 6, No. 1, 8379, Sep. 2015.
- [32] Liu, C., S. Wang, S. Zhang, Q. Cai, P. Wang, C. Tian, L. Zhou, Y. Wu, and Z. Tao, “Active spintronic-metasurface terahertz emitters with tunable chirality,” *Advanced Photonics*, Vol. 3, No. 5, 056002, Oct. 2021.
- [33] Liu, M., E. Plum, H. Li, S. Duan, S. Li, Q. Xu, X. Zhang, C. Zhang, C. Zou, B. Jin, J. Han, and W. Zhang, “Switchable chiral mirrors,” *Advanced Optical Materials*, Vol. 8, No. 15, 2000247, Aug. 2020.
- [34] Zhu, Z., Z. Qin, H. Wang, L. Jiang, Y. Li, W. Wang, H. Chen, J. Wang, Y. Pang, and S. Qu, “Switchable chiral mirror based on PIN diodes,” *Photonics Research*, Vol. 11, No. 7, 1154–1161, Jul. 2023.
- [35] Menzel, C., C. Rockstuhl, and F. Lederer, “Advanced Jones calculus for the classification of periodic metamaterials,” *Physical Review A*, Vol. 82, No. 5, 053811, Nov. 2010.
- [36] Katsarakis, N., T. Koschny, M. Kafesaki, E. N. Economou, and C. M. Soukoulis, “Electric coupling to the magnetic resonance of split ring resonators,” *Applied Physics Letters*, Vol. 84, No. 15, 2943–2945, Apr. 2004.
- [37] Landy, N. I., S. Sajuyigbe, J. J. Mock, D. R. Smith, and W. J. Padilla, “Perfect metamaterial absorber,” *Physical Review Letters*, Vol. 100, No. 20, 207402, May 2008.
- [38] Li, B. and Z. Shen, “Synthesis of quasi-elliptic bandpass frequency-selective surface using cascaded loop arrays,” *IEEE Transactions on Antennas and Propagation*, Vol. 61, No. 6, 3053–3059, Jun. 2013.
- [39] Zhao, P.-C., Z.-Y. Zong, W. Wu, and D.-G. Fang, “A convoluted structure for miniaturized frequency selective surface and its equivalent circuit for optimization design,” *IEEE Transactions on Antennas and Propagation*, Vol. 64, No. 7, 2963–2970, Jul. 2016.
- [40] Saifullah, Y., G. Yang, and X. Feng, “A four-leaf clover-shaped coding metasurface for ultra-wideband diffusion-like scattering,” *Journal of Radars*, Vol. 10, No. 3, 382–390, Jun. 2021.
- [41] Droulias, S., “Chiral sensing with achiral isotropic metasurfaces,” *Physical Review B*, Vol. 102, No. 7, 075119, Aug. 2020.
- [42] Khoo, E. H., E. S. P. Leong, S. J. Wu, W. K. Phua, Y. L. Hor, and Y. J. Liu, “Effects of asymmetric nanostructures on the extinction difference properties of actin biomolecules and filaments,” *Scientific Reports*, Vol. 6, No. 1, 19658, Jan. 2016.